GEOFLUIDS

Geofluids (2015) doi: 10.1111/gfl.12151

Modelling the Lost City hydrothermal field: influence of topography and permeability structure

S. S. TITARENKO AND A. M. MCCAIG

Institute for Geophysics and Tectonics, School of Earth and Environment, University of Leeds, Leeds, UK

ABSTRACT

The Lost City hydrothermal field (LCHF) is hosted in serpentinite at the crest of the Atlantis Massif, an oceanic core complex close to the mid-Atlantic Ridge. It is remarkable for its longevity and for venting low-temperature (40–91°C) alkaline fluids rich in hydrogen and methane. IODP Hole U1309D, 5 km north of the LCHF, penetrated 1415 m of gabbroic rocks and contains a near-conductive thermal gradient close to 100°C km^{-1}. This is remarkable so close to an active hydrothermal field. We present hydrothermal modelling using a topographic profile through the vent field and IODP site U1309. Long-lived circulation with vent temperatures similar to the LCHF can be sustained at moderate permeabilities of 10^{-14} to 10^{-15} m^2 with a basal heatflow of 0.22 W m^{-2}. Seafloor topography is an important control, with vents tending to form and remain in higher topography. Models with a uniform permeability throughout the Massif cannot simultaneously maintain circulation at the LCHF and the near-conductive gradient in the borehole, where permeabilities $<10^{-16}$ m^2 are required. A steeply dipping permeability discontinuity between the LCHF and the drill hole is required to stabilize venting at the summit of the massif by creating a lateral conductive boundary layer. The discontinuity needs to be close to the vent site, supporting previous inferences that high permeability is most likely produced by faulting related to the transform fault. Rapid increases in modelled fluid temperatures with depth beneath the vent agree with previous estimates of reaction temperature based on geochemical modelling.

Key words: Atlantis Massif, finite element model, fluid flow, hydrothermal, IODP Hole 1309D, Lost City, mid-Atlantic Ridge, oceanic core complex, permeability

Received 13 February 2015; accepted 30 July 2015

Corresponding author: Andrew M. McCaig, School of Earth and Environment, University of Leeds, Leeds LS2 9JT UK. Email: a.m.mccaig@leeds.ac.uk. Tel: +44 113 3435219. Fax: +44 113 3435259.

Geofluids (2015)

INTRODUCTION

The Lost City hydrothermal field (LCHF) was discovered in the year 2000 (Kelley *et al.* 2001). It is located near the highest point of the Atlantis Massif (Fig. 1), an inside corner high north of the Atlantis transform fault. The Atlantis Massif has been interpreted as an oceanic core complex since the discovery of spreading parallel corrugations on its surface (Cann *et al.* 1997; Blackman *et al.* 1998). The south wall of the massif has been investigated extensively by dredging and submersible studies (Schroeder & John 2004; Boschi *et al.* 2006; Karson *et al.* 2006) and consists mainly of serpentinized peridotite with subordinate gabbro, often mylonitized. The Massif is capped by a 100-m-thick shear zone consisting of foliated serpentinite and talc–tremolite–chlorite schist overlain by a carbonate-cemented breccia. This shear zone is interpreted as a convex-upward detachment fault which exhumed gabbro and peridotite onto the seafloor, with deformation predominantly in the greenschist facies (Boschi *et al.* 2006; McCaig *et al.* 2010).

Five km to the north of the LCHF is IODP Hole U1309D, drilled in Expeditions 304 and 305 in 2004/2005 (Blackman *et al.* 2006, 2011; Ildefonse *et al.* 2007). This penetrated 1415 metres below seafloor (mbsf) and recovered predominantly gabbroic rocks, in contrast to the peridotite-dominated south wall of the Massif. The gabbros are almost completely undeformed in the ductile regime, but are strongly altered to greenschist and amphibolite facies assemblages. A few samples of talc–tremolite–chlorite schist recovered within 20 m of the seafloor, and breccia zones cut by diabase intrusions within the top 100 m of the Hole, are interpreted as the detachment fault (Blackman *et al.* 2006, 2011; McCaig *et al.* 2010). McCaig & Harris (2012) suggested that the high proportion of diabase in the upper part of the Hole is because it acted as a local dike-gabbro transi-

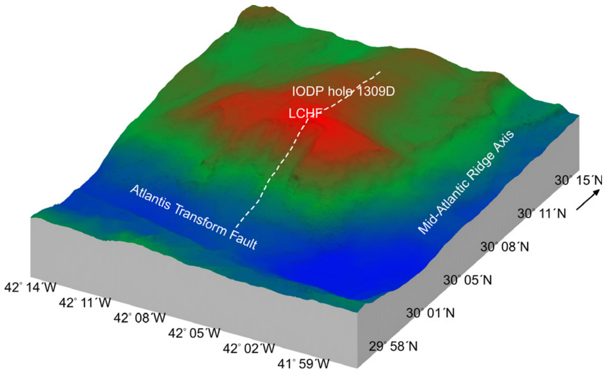

Fig. 1. 3-D image of the Atlantis Massif showing the Lost City hydrothermal field (LCHF) and IODP Hole U1309D, together with our N–S model profile. Topography was extracted from a GMT file supplied by Donna Blackman.

tion zone and conductive boundary layer during faulting, at a time when the detachment fault was an upflow zone for black smoker fluids. This inferred earlier phase of hydrothermal circulation was unrelated to the LCHF (Boschi *et al.* 2006; McCaig *et al.* 2010).

IODP Hole U1309D was revisited in early 2012 during IODP Expedition 340T. The Hole was relogged using a variety of tools including temperature (Blackman *et al.* 2013), and a thermal gradient of ~100°C km^{-1} was recorded (see Figure S1). The gradient is linear below 750 mbsf, indicating conductive heat transfer, and slightly curved above 750 mbsf indicating slow downward advection of seawater at about 1 cm year^{-1} (Blackman *et al.* 2014).

The Lost City hydrothermal field is located on a down-faulted terrace just south of the highest point of the Massif and is remarkable for forming carbonate–brucite chimneys up to 60 m high. The Field consists of a complex grouping of chimneys, in an area of about 500 m^2 (Kelley *et al.* 2001, 2005; Früh-Green *et al.* 2003; Ludwig *et al.* 2011). Most authors consider that the location of the field is controlled by E-W faulting related to the Atlantis Transform Fault, coupled with a cross-fault trending 020° (Kelley *et al.* 2005; Karson *et al.* 2006). While faults clearly control the immediate vent site, it is not clear whether flow is confined within faults at depth. Collins *et al.* (2012) studied the seismicity of the Massif, which is dominated by small earthquakes of magnitude 2 or less. Earthquakes occur in the transform valley and the south wall of the Massif, including the vicinity of the LCHF but mainly further east. A N-facing fault scarp north of the LCHF is seismically active and may be a strike slip fault. There is no current seismicity at the location of IODP Hole U1309D.

The system shows unique properties and differs from black smoker systems in having relatively low vent temperatures (40–91°C), high concentrations of H_2 and CH_4 in the upflowing fluids (Kelley *et al.* 2005; Proskurowski *et al.* 2006) and unusual longevity of at least 120 000 years on the basis of ^{230}Th dating (Ludwig *et al.* 2011). Zircon ages from IODP Hole U1309D, 5 km north of the LCHF, range from 1.08 to 1.28 Ma with a mean of 1.2 ± 0.03 Ma (Grimes *et al.* 2008). These ages are younger than previous estimates of the age of the Massif (Blackman *et al.* 2002) suggesting asymmetric spreading. The age of the Massif coupled with the low vent temperatures suggests that a magmatic heat source beneath Lost City is unlikely. Several authors (Lowell & Rona 2002; Früh-Green *et al.* 2003; Kelley *et al.* 2005; Emmanuel & Berkowitz 2006; Kelley & Shank 2010) have considered that heat from exothermic serpentinization of olivine, in addition to heat contained within the Massif, may contribute significantly to driving the circulation. However, Allen & Seyfried (2004) argued that a significant role for heat of serpentinization would require low water–rock ratios, which are inconsistent with the chemistry of Lost City vent fluids. Allen & Seyfried (2004) and Seyfried *et al.* (2015) also suggested that temperatures of around 200°C, far higher than measured vent temperatures, are required at shallow depths beneath the LCHF to explain vent fluid chemistries. Foustoukos *et al.* (2008) estimated reaction temperatures of around 250°C for the vent fluids, again requiring significant conductive cooling during ascent to the seafloor.

The majority of models of seafloor hydrothermal circulation focus on relatively short-lived black smoker vent systems driven by magmatic heat sources; the development of models in such systems has been recently reviewed (Ingebritsen *et al.* 2010). The first simulations used simple water properties (constant viscosity and density linearly dependent on T) and square or rectangular domains (Kimura *et al.* 1986; Graham & Steen 1994; Cherkaoui & Wilcock 1999, 2001). Further papers showed the importance of using temperature-dependent viscosity and density without the Boussinesq approximation (Ingebritsen & Hayba 1994; Wilcock 1998; Coumou *et al.* 2006; Fontaine & Wilcock 2007). Coumou *et al.* (2009) have calculated 3-D models of mid-ocean ridge hydrothermal systems using realistic water properties.

Numerical models relevant to off-axis, cooler systems such as Lost City are less common. Fisher & Becker (2000) modelled long-range flow through shallow crustal aquifers confined by sediment, an approach extended to 2-D by Anderson *et al.* (2012). Some models have shown the importance of topography in such systems (Harris *et al.* 2004; Kawada *et al.* 2011). Topography has also been included in some black smoker modelling (Schardt *et al.* 2006; Schardt & Large 2009). No explicit models of the LCHF have been published, although Emmanuel & Berkowitz (2006) constructed generic 2-D models of the effects of serpentinization on systems at a range of temperatures. Our models are the first to include the effects of topography, or the important constraint of the nearby borehole temperature profile.

Here, we present a series of numerical models using a 2-D profile of the real topography along a N–S line passing through the LCHF and very close to IODP Hole U1309D (Figs 1 and 2), using COMSOL multiphysics. The combination of measured vent temperatures and nearby borehole thermal measurements provides much stronger constraints on circulation models than is usual in oceanic systems. We show that topography and permeability structure are the main controls on vent location, and can place limits on the bulk permeability of both gabbro beneath IODP Site U1309, and fractured serpentinite beneath the LCHF.

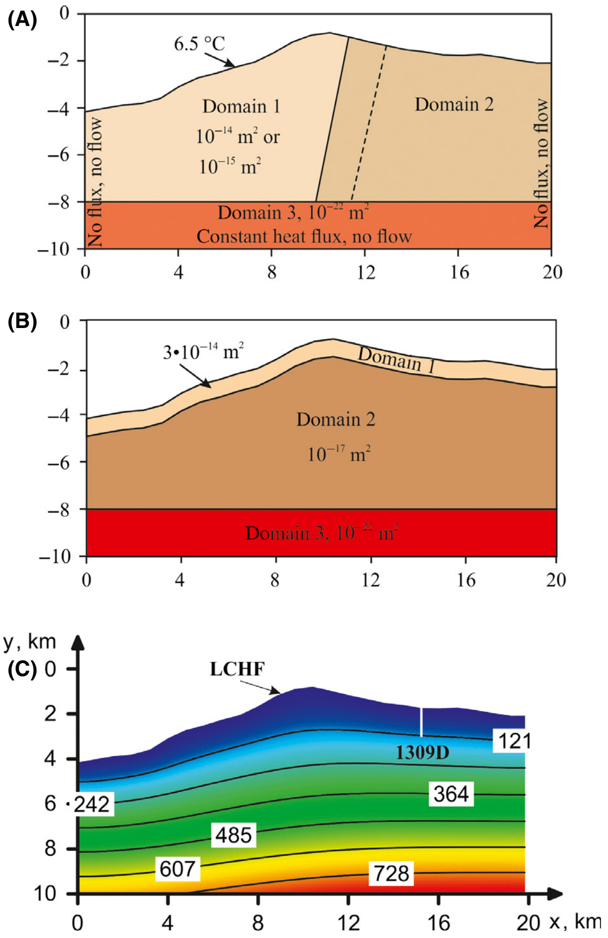

Fig. 2. (A) Model setup and boundary conditions. Domains 1 and 2 can have different permeabilities, while domain 3 has a permeability of 10^{-22} m^2 in all models. Solid line shows the domain 1–domain 2 boundary for Model B, dashed line for model C. Top boundary condition of 6.5°C corresponds to best estimates of the sea bottom temperature at IODP Site U1309 (Gilles Guerin *pers comm.*, 2013; Blackman *et al.* 2013). Topography was extracted from a GMT file supplied by Donna Blackman and smoothed using Fourier series. (B) Model D geometry and permeabilities (C) Initial temperature structure (in °C) for all models, corresponding to a purely conductive model at steady state.

We have applied our models primarily to the Atlantis Massif because the unique combination of a deep borehole thermal profile in proximity to a well-studied hydrothermal field makes it the best studied such system in the oceans. However, our models have a generic application to flow of fluid in exhumed oceanic core complexes and topographic massifs. In particular, we show that a steeply dipping permeability contrast into a conductive regime creates a lateral thermal boundary layer which stabilizes venting at approximately constant temperature over time periods $> 10^5$ years, if the permeability required for advective circulation can be maintained.

MODEL SET UP

Rationale

Lost City is a long-lived system, which has been producing carbonate chimneys for at least 120 ka in approximately the same location (Ludwig *et al.* 2011). We aim to investigate the influence of topography and permeability structure on the location and stability of the vent field, and on vent temperatures, while maintaining observed temperature conditions in IODP Hole 1309D. Figure 2 shows our model geometry; we used a slightly smoothed version of the real topography along a N–S transect through Lost City, which also passes very close to the location of IODP Hole 1309D. Three different domains are assigned variable permeabilities in different models. To reproduce conditions at the LCHF, we aim to produce a quasi-steady state with venting in a stable position near the crest of the Massif over periods in excess of 120 kyr.

Boundary conditions

In the majority of our models, we have used a constant heat flow lower boundary condition of $0.22\ \mathrm{W\ m^{-1}}$ which gives a good match to the basal temperature measured in the borehole in a purely conductive model. This may be an underestimate of the true heatflow (Blackman *et al.* 2014). For low temperature off-axis circulation, this boundary condition is much more realistic than the constant temperature boundary condition generally used in magmatic-hydrothermal models. In hydrothermal circulation modelling, there are two possible top boundary temperature conditions:

(1) Mixed boundary conditions which are sensitive to the velocity field orientation and mathematically can be written in the form:

$$\begin{cases} T = 0, & \text{fluid flowing in,} \\ \frac{\partial T}{\partial n} = 0, & \text{fluid flowing out} \end{cases} \tag{1}$$

(2) Dirichlet boundary conditions which fix temperature on the upper boundary to a constant value.

Neither of these conditions is physically correct. The mixed condition allows estimation of vent temperatures in a straightforward way and is commonly used in modelling black smoker systems (Emmanuel & Berkowitz 2006; Fontaine & Wilcock 2007; Coumou *et al.* 2009). However, because no conductive heat loss is possible through the top boundary in regions of upward flow, the seafloor can become unrealistically hot in regions of persistent slow upward flow. This may not be a problem in black smoker models where advective heat flux is high and model duration short, but in our models lasting up to 1 million years, large areas of seafloor reached temperatures of over 30°C. In addition, models using this boundary condition were extremely noisy and unexplained jumps in vent temperature occurred, probably due to temperature switching in boundary elements. This appears to have been exacerbated by the inclusion of seafloor topography, as early test models in a square box were more stable.

The Dirichlet condition requires fluids to vent at a constant low temperature, and therefore cool rapidly in the model through an upper boundary layer. Vent temperatures cannot be extracted directly. Wilcock (1998) showed that vent temperature can be estimated by a linear extrapolation from depth. He compared the two boundary conditions and showed that the Dirichlet condition gives somewhat higher vent temperatures, suggesting that the real vent temperatures should be somewhere in between these values and those obtained with Neumann boundary conditions. Importantly, he showed that the choice of boundary condition did not significantly affect the form or time dependence of circulation, mass fluxes or Nusselt numbers other than in the top boundary layer.

In the models presented here, we have used the Dirichlet boundary condition with a seafloor temperature of 6.5°C (Fig. 2A), corresponding to best estimates of the sea bottom temperature at IODP Site U1309 (Gilles Guerin *pers. comm.*, 2013; Blackman *et al.* 2013). To estimate the vent temperature, we extracted maximum temperature as a function of depth from the COMSOL output and used linear extrapolation as suggested by Wilcock (1998). At high flow rates, a clear inflexion in the temperature profile of the ascending fluid occurs and extrapolation is straightforward. At lower flow rates, this inflexion becomes less defined, and vent temperatures more uncertain; this occurs at low permeabilities and in the later stages of some models. At low flow rates, fluid mixing undoubtedly occurs in nature (Wilcock 1998) and cannot easily be simulated. Therefore, modelled vent temperatures are probably in general overestimated compared to measured ones.

We allow fluid to move through the upper boundary only, with the bottom and sides impermeable (Fig. 2A).

Initial conditions

Initial temperature has been calculated by solving the purely conductive problem over the whole domain. Setting the basal heat flux to 0.22 W m^{-1} and temperature on the seafloor to 6.5°C, we get the initial temperature distribution shown in Fig. 2B. This means that in the early stages of convection, large amounts of heat are released from the higher permeability domains, before the models reach a quasi-steady state lasting for >120 ka. It is this second phase of relatively low temperature circulation that we consider to be significant; in this phase, temperatures of circulating fluid are invariably <300°C, and high temperatures in the early part of model runs are an artefact of the initial conditions. It would have been possible to use initial conditions of uniform low temperature, but very long model times would be required to match the near-conductive regime seen in Hole 1309D, and the early part of model runs would be equally insignificant.

The initial conditions for pressure have been found according to the definition $P(x, y) = g \cdot \int_{y_0}^{0} \rho(x, y)dy$. The function $\rho(x, y)$ is calculated using the initial temperature field and T-dependent profile of the function $\rho(T)$ (see Figure S2).

Governing equations

The problem has been calculated on a quadro core workstation with COMSOL multiphysics software using the Heat Transfer and Subsurface Flow Modules. The domain has been discretized by a Delaunay triangulation technique. For vent temperature estimation in the Dirichlet boundary condition, we used an additional program written in C++, and the method of Wilcock (1998). For most models, the maximum vent temperature at any time was extracted by searching for the highest upflow temperatures, but for two models (B14A and B14B), a less sophisticated algorithm was used that calculated vent temperature at the final, stable vent position only. We used pure water properties (see Figure S2), calculated according to the international steam tables IAPWS-IF97 (Wagner & Kretzschmar 2008). The functions are dependent both on temperature and pressure and have a discontinuity in the region of phase separation. There is no evidence for phase separation at Lost City. Vent temperatures are in the range 40–90°C, and maximum temperatures of circulation are about 250°C (Allen & Seyfried 2004). At the pressure of venting (~80 MPa), temperatures of about 300°C are required for boiling of seawater (Anderko & Pitzer 1993). There is therefore no need to consider phase separation in the low temperature circulation periods of our models that we consider to be representative of circulation at Lost City. However, it could occur in the initial transient high-temperature circulation in our models as heat is removed from the initial conditions, and therefore needs to be dealt with in some way. Previous authors have addressed this using an enthalpy formulation for the governing equations (Ingebritsen & Hayba 1994; Ingebritsen *et al.* 2010), by averaging the properties of the two phases in the supercritical region (Wilcock 1998; Fontaine & Wilcock 2007), or using pure water at pressures above the critical point of 22.1 MPa. It is difficult to implement the enthalpy formulation in COMSOL Multiphysics. The water depth at Lost City is only 780 m, so artificially high seafloor pressures are required to exclude boiling from the models. Initially, we used the Coumou *et al.* (2009) approach, fixing the pressure at the summit of the Massif at 25 MPa, but our model runs of up to 1 myr were very time-consuming, and often unstable (note that the inclusion of topography adds significantly to computation times compared to rectangular domains of the same permeability). As water properties were already approximated by the use of pure water and the unrealistic pressure condition, we adopted a simplified approach by calculating pure water properties along an isobar at 50 MPa (Fig. S2), corresponding to the middle of the model (Fig. 2). Over the temperature range of 0–300°C experienced by Lost City fluids, the effects of pressure on water density and viscosity are small compared to those of temperature (Wagner & Kretzschmar 2008), and pure water properties show very similar temperature dependence to seawater (Pitzer *et al.* 1984; Anderko & Pitzer 1993). A comparison of water properties using our isobaric formulation and a P-T-dependent formulation is presented in Table S1. Therefore, the vent system can be described by a set of equations for one phase:

$$\begin{cases} \rho_f(T)C_{pf}(T)\varepsilon+\rho_p C_{pp}(T)(1-\varepsilon)\dfrac{\partial T}{\partial t}(x,y,t)+\rho_f(T)C_{pf}(T) \\ \mathbf{v}\cdot\nabla T(x,y,t)=\nabla\cdot((k_p(T)(1-\varepsilon)+k_f\varepsilon)\nabla T(x,y,t)), \\ \mathbf{v}=-\dfrac{k(T)}{\mu(T)}(\nabla p(\rho_f(T))+\rho_f(T)\mathbf{g}), \\ \dfrac{\partial}{\partial t}(\rho_f\varepsilon+\nabla\cdot(\rho_f\mathbf{v})=0) \end{cases}$$

Here, rock properties $C_{pp}(T)$, $k_p(T)$ and $k(T)$ are temperature-dependent functions (Seipold 1998; Bouhifd *et al.* 2007). For conductivity, equation (9) of Seipold (1998) was used together with the mean room temperature value for gabbro and olivine gabbro/troctolite reported by Blackman *et al.* (2006). See Figure S3 for graphs of $C_{pp}(T)$ and $k_p(T)$. The corresponding range of thermal diffusivity is $(1.088-0.559) \times 10^{-6}$ m^2 sec^{-1}. A rock density of 2900 kg m^{-3} was assumed, which is the average value measured in IODP Hole 1309D (Blackman *et al.* 2013).

We used temperature-dependent permeability functions designed to simulate ductile closure of cracks at high temperature (Hayba & Ingebritsen 1997; Coumou *et al.* 2009). The permeability falls to 10^{-22} m^2 at temperatures of 800°C from a value below 600°C which is model-dependent (see Figure S4), simulating a brittle–ductile transition at ~700°C. All models have a basal layer 2 km thick with a constant permeability of 10^{-22} m^2, which keeps hydrothermal fluid away from the lower boundary condition. Topography was extracted from a GMT file supplied by Donna Blackman and smoothed using Fourier series.

Discretization

The problem has been solved on a domain 20 km in length and 10 km in depth from sea level. For discretization, we used a Delaunay triangulation algorithm. We applied a non-uniform grid, refining the mesh size for the domains with more vigorous convection. Further details of the numerical methods can be found in the supporting material, together with details of the mesh size for the various models (Table S2).

Model permeability structures

The permeability structure of the Massif plays a dominant role in controlling patterns of hydrothermal circulation and is the principle parameter varied in our models (Fig. 2A). In all models, domain 3 has a low permeability of 10^{-22} m^2 designed to suppress hydrothermal circulation close to the basal boundary condition. Models are designed to test the effects of topography and different permeability structures based on the known geology of the Massif, and are defined as follows:

Model A

In this model, domains 1 and 2 (Fig. 2A) have equal permeability, varying between 10^{-15} and 10^{-14} m^2, with the temperature-dependent permeability function shown in the supporting material in each case. This model is designed to investigate the effect of topography alone on circulation. Models at different permeabilities are called A15 and A14.

Model B

In this model, the permeability of domain 2, which includes the drill hole, is reduced to $k = 10^{-17}$ m^2, whereas in domain 1 higher permeability of 10^{-15} and 10^{-14} m^2 (models B15 and B14, respectively) allows vigorous hydrothermal circulation. The boundary between domains 1 and 2 was chosen to simulate higher permeability in a zone beneath the southern slope of the Massif assumed to be affected by active faulting along the Atlantis transform fault (Kelley *et al.* 2005; Karson *et al.* 2006; Collins *et al.* 2012). A version of Model B (model B14A) was also used in which domain 3 was 4 km thick, providing for a shallower zone of circulation, while model B14B used a higher basal heatflow of 0.24 W m^{-2}.

Model C

This model is identical to model B except that the boundary between domains 1 and 2 is located further to the north, corresponding approximately to the steeply dipping boundary between high and low seismic velocity domains seen in seismic tomography (Canales *et al.* 2008; Henig *et al.* 2012). This boundary has been inferred to mark the transition from a gabbroic domain beneath the borehole to a serpentinized peridotite domain beneath the LCHF.

Model D

This model (Fig. 2) has a 750-m-thick layer of higher permeability parallel to the topography. It was designed to try and match the evidence for slow downflow of water in the top 750 m of IODP Hole 1309D (Blackman *et al.* 2014). This model was only run at a single permeability (3×10^{-14} m^2) as it was realized that 3-D models were required to fully match the borehole temperature profile and heatflow into the Massif (Titarenko & McCaig 2014b, and in prep.), but vent temperatures were calculated which are relevant to the current paper.

RESULTS

Model A

In model A, we tried different values of permeability in a combined domain covering the upper part of the Massif. Movie S1 and Fig. 3 show how the thermal structure of the massif evolves with time at illustrative permeabilities of 10^{-15} and 10^{-14} m^2. The thermal structure is a good proxy for flow patterns, with high temperatures indicating upflow and low temperatures downflow zones. The movies (Movie S1 and S2) show that in each case the first vents form close to the site of the LCHF at the crest of the Massif and are high temperature (>220°C). This transient high-temperature phase reflects removal of heat from the conductive initial condition, which is unlikely ever to have occurred over the whole Massif, and we do not consider it to be significant. The conditions at Lost City are more likely to correspond to the subsequent phase of relatively stable, lower temperature venting, as seen in the snapshots at longer times (Fig. 3). With time, the vents merge and split and migrate backwards and forwards over the higher part of the model, including the location of the drill hole. At the higher permeability value, the circulation is more unstable, with more vents and a quicker decay of the initial high-temperature venting regime, but the essential pattern is similar. However, in both cases of 10^{-15} and 10^{-14} m^2, by the end of 0.5 m.y., the main vent gradually moves to the right-hand side of the domain. We see the main vent is unlikely to stay for a long time in the location of Lost City. At IODP Site U1309, flow in the model can be either upward or downward but the gradient is never conductive.

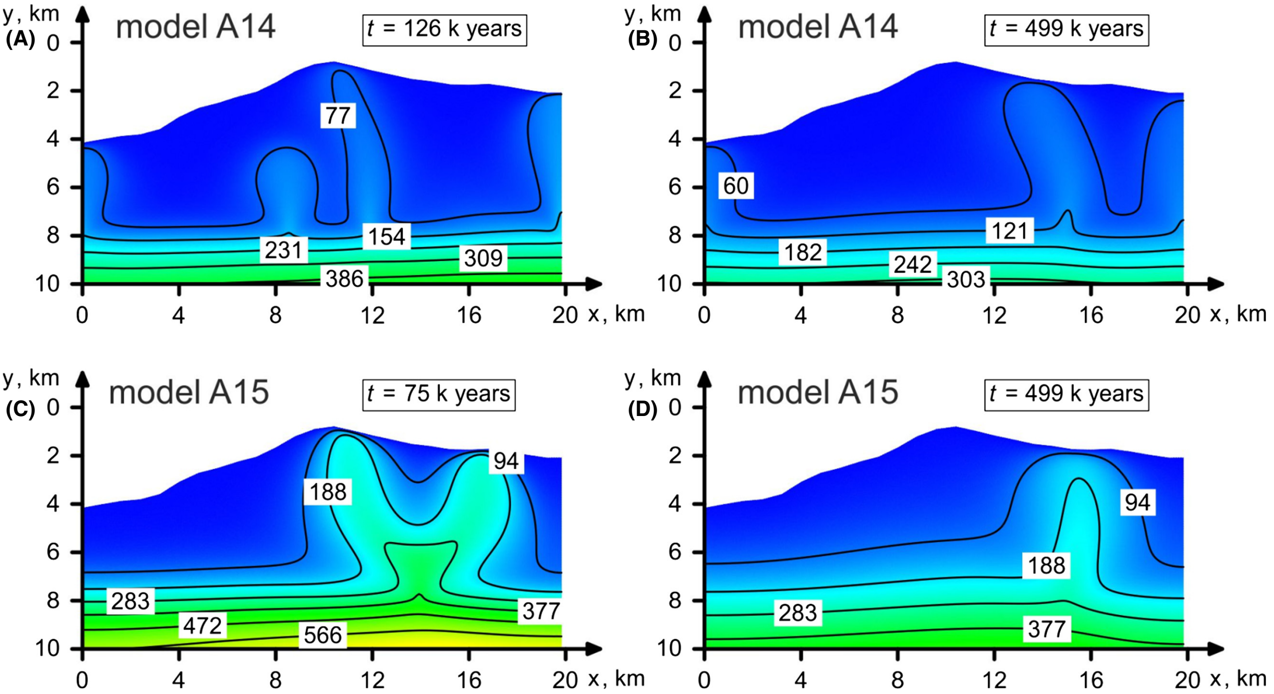

Fig. 3. Snapshots of temperature structure in Model A14 (A and B) and A15 (C and D) at intermediate times and the end of the run. For the initial transient phase of high-temperature venting (which is not considered significant for the LCHF), see the videos in Movie S1 and S2.

Figure 4 shows the Darcy velocity field for model A15 during the period of steady venting. Fluid enters the model through the seafloor everywhere except the single vent region, and there is significant recirculation of fluid within the model in the flanks of the vent. Maximum Darcy flow velocities of 10^{-8} m $\sec^{-1}$ are in the upwelling vent region somewhat below the seafloor.

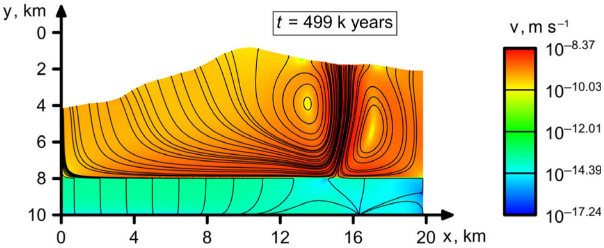

Fig. 4. Darcy velocity field after 500 000 years for model A15.

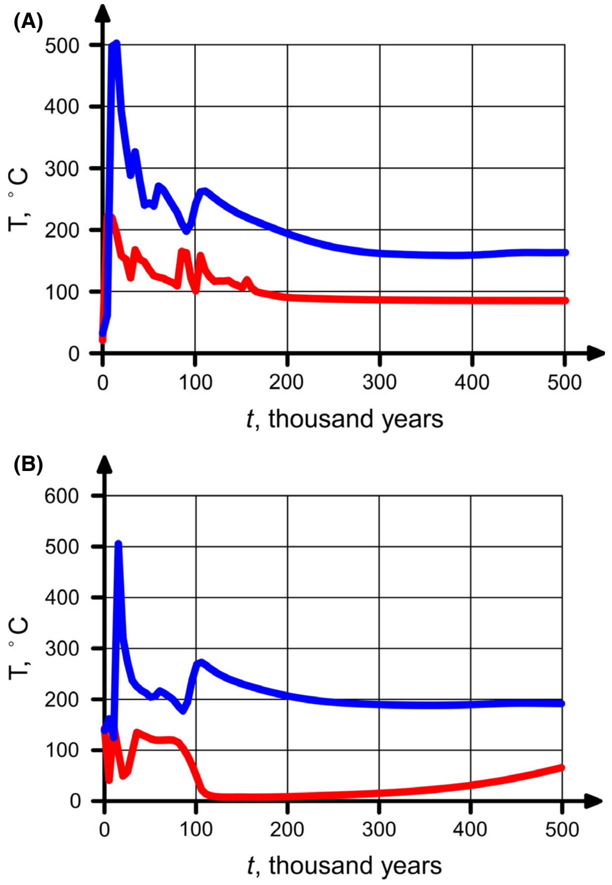

Fig. 5. (A) Estimated vent temperatures for models A14 (red) and A15 (blue) as a function of time. Note that the initial phase of high-temperature venting represents removal of heat from the initial condition and is not considered relevant to the LCHF (B) Temperature at a depth of 1415 mbsf at the location of IODP Hole U1309D for models A14 (red) and A15 (blue). The measured temperature at that depth is 146°C (Blackman *et al.* 2013).

Figure 5A shows the estimated vent temperature as a function of time for both permeabilities. At higher permeability, cooling is much more rapid resulting in a lower main vent temperature (the main vent at any time is that with the maximum temperature of upwelling fluid). At a permeability of 10^{-14} m^2, vent temperatures at the LCHF are approximately matched over long periods. At lower permeability, the vent temperature never reaches the observed range of 40–91°C.

Figure 5B shows the temperature at a location corresponding to the bottom of IODP Hole U1309D. The temperature gradient changes rapidly with time and can be either higher or lower than that measured (~100°C km^{-1}). When vents are located close to the LCHF, flow at the borehole is generally strongly downwards, leading to much lower temperatures at the borehole than measured. When vents cross the borehole site, the borehole gradient is greater than observed. It is evident that the measured and modelled borehole bottom temperatures could only match for very short periods of time, and the near-linear measured gradient is very unlikely ever to be matched.

Model B

In model B, domain 2, beneath the borehole, has a permeability of 10^{-17} m^2, which almost completely suppresses hydrothermal circulation in this domain. In domain 1, fluid enters the seafloor in the transform valley and rises up the domain boundary to vent very close to the LCHF (Fig. 6). For a movie, see Movie S3. This pattern is established very quickly in the models and persists to times of 1 m.y. Figure 7 shows the flow patterns and Darcy velocities for model B14 after 0.5 m.y. The asymmetry of circulation compared to model A is clear, and recirculation only occurs on one flank of the vent. With the exception of the southern edge of the model, fluid enters the seafloor everywhere except the main vent site located at the LCHF including domain B where downflow is nevertheless too slow to produce the slightly curved measured temperature profile (see Blackman *et al.* (2014)).

Figure 8A shows estimated vent temperatures for the structures B14 and B15 as a function of time. In both cases, an initial transient period of high-temperature venting (which is not considered significant as discussed above) is followed by a long period of slowly declining temperatures, somewhat higher at the lower permeability. As discussed above, it is likely that these temperatures are slightly overestimated due to the use of the Dirichlet boundary condition, while fluid mixing at shallow levels probably means that the measured vent temperatures of 41–90 °C are lower than would be expected in our model, which does not allow mixing. Figure 8B shows the borehole temperature at 1415 m as a function of time, while Figure 8C shows the thermal gradient in the borehole at two

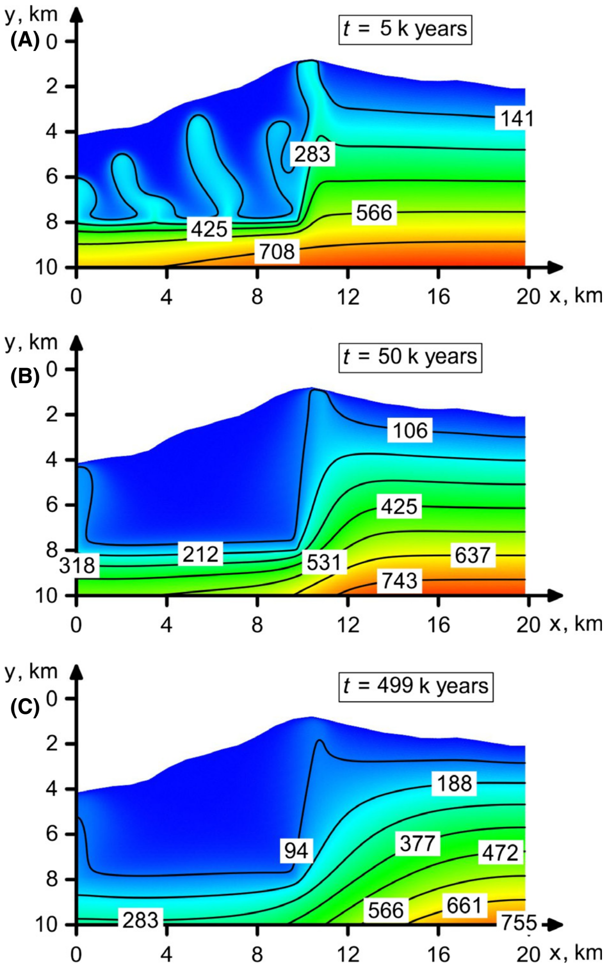

Fig. 6. Snapshots of the temperature structure in model B14 at short (A), intermediate (B) and long (C) times. For the temperature evolution, see Movie S3.

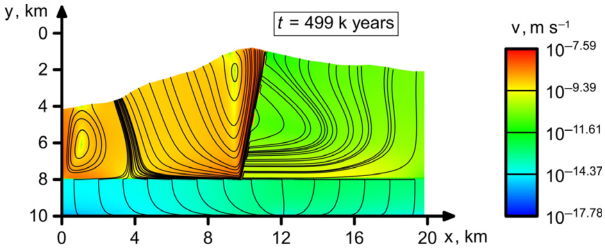

Fig. 7. Darcy velocity field in model B14 after 500 000 years.

moments of time compared with the measured gradient. It is evident that in model B the borehole gradient can be approximately matched over long periods of time, but the model gradient is more linear than the observed one. The borehole gradient can be matched more closely (see model D) by slow downflow of fluid at that location in the upper 750 m of the domain (Blackman *et al.* 2014); further modelling is in progress which demonstrates this (Titarenko & McCaig 2014b, and in prep.).

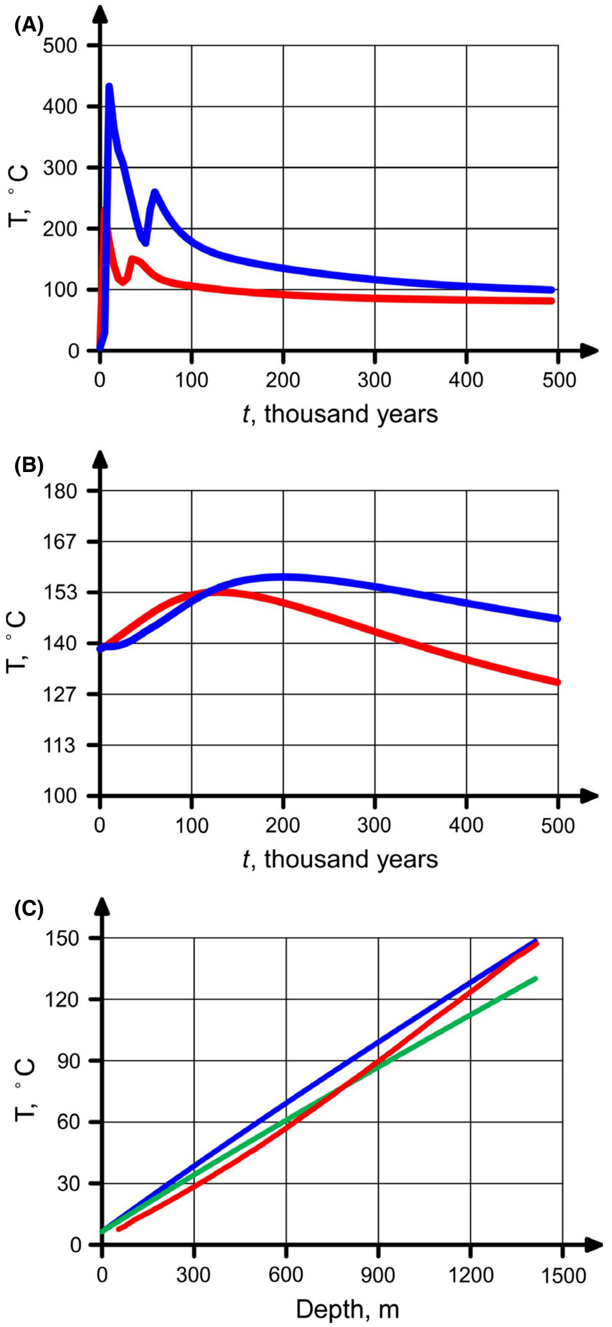

Fig. 8. (A) Estimated vent temperatures for model B14 (red) and B15 (blue) as a function of time. Note that the initial phase of high temperature venting represents removal of heat from the initial condition and is not considered relevant to the LCHF (B) Temperature at a depth of 1415 mbsf at the location of IODP Hole U1309D for models B14 (red) and B15 (blue). (C) Temperature gradient at the site of IODP Hole U1309D for model B14 after 230 000 years (blue) and after 500 000 years (green). Red line is the measured gradient (Blackman *et al.* 2013).

In an early model, we used a higher basal heatflow of 2.4 W m^{-2} at a permeability of 10^{-14} m^2. This leads to a somewhat higher vent temperature (Fig. 10).

Model C

In this model, the boundary between domains 1 and 2 is shifted to the north, while maintaining the permeability structure of model B. Figure 9 shows that the pattern of circulation is very similar to model B, but the final location of the vent is controlled more by the permeability barrier than the topography of the massif, and is located about 2 km north of the site of the LCHF. Vent temperatures are slightly higher than the corresponding values in model B (Fig. 10), and the borehole gradients are very similar.

Model D

The pattern of circulation in this model is shown in Fig. 11A. Fluid rises at the location of the LCHF and also in a small hill north of IODP Hole 1309D, and sinks at the location of the borehole. Vent temperatures (Fig. 11B) are ~ 14°C at a permeability of 3×10^{-14} m^2. Although a reasonable match to the temperature profile in the borehole is obtained at the above permeability and a basal heatflow of 2.22 W m^{-2} (Fig. 11C), 3-D modelling (Titarenko & McCaig 2014b and in prep.) suggests that somewhat higher values of both permeability and heat flow are required.

DISCUSSION

Effects of topography

Previous models including seafloor topography have generally studied seamounts on ridge flanks in Pacific crust, although some topographic models of black smoker systems have been made (Schardt *et al.* 2006; Schardt & Large 2009). Harris *et al.* (2004) showed that in unconfined models, upflow normally focuses in the highest topography, with subsidiary vents on seamount flanks. This is a similar result to ours, but with higher permeability, less extreme topography, and a lower basal heat flow. Kawada *et al.* (2011) modelled a bare seamount surrounded by impermeable sediment covering a permeable basaltic layer. In their models, large seamounts tended to act as recharge zones for circulation once they had cooled by circulation within the seamount. However, they only modelled one seamount, with an open lateral boundary to the model and no means to introduce cold fluid into the seafloor other than through the central seamount. Observations on ridge flanks (Fisher & Becker 2000; Anderson *et al.* 2012) suggest that some seamounts act as recharge zones while others act as discharge zones, with flow through a shallow confined aquifer in the uppermost basalts, but the controls

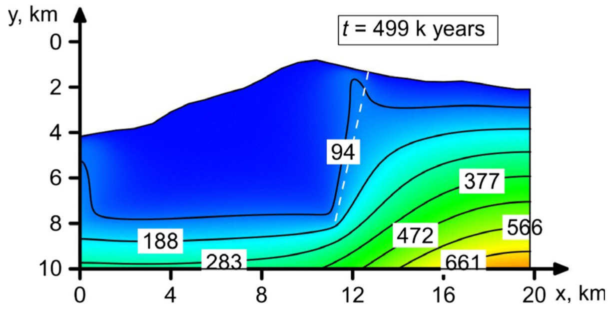

Fig. 9. Snapshot of the thermal structure in model C14 after 500 000 years. Note the similarity to model B14, other than vent location. The dashed line is the boundary between domains 1 and 2. For a video of this model, see Movie S4.

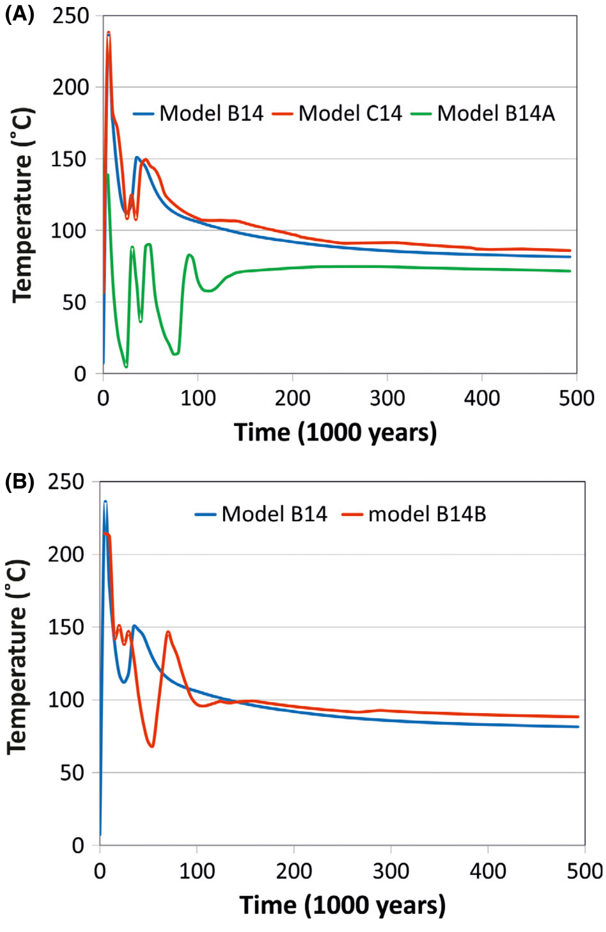

Fig. 10. (A) Comparison of model C14 (Fig. 9) vent temperatures with model B14 and with model B14A, in which domain 3 (Fig. 2) was 4 km thick rather than 2 km in model B14. (B) Comparison of model B14 vent temperatures (Fig. 8) with model B14B, in which basal heatflow was 0.24 W m^{-2} compared with 0.22 W m^{-2} in model B14. Note that models B14A and B14B used a less sophisticated algorithm for estimating vent temperatures where the procedure suggested by Wilcock (1998) was applied at the final, stable vent position throughout, rather than at the location of main venting identified by the highest fluid temperatures near the seafloor. Hence, low temperatures are seen in the initial unstable vent phase.

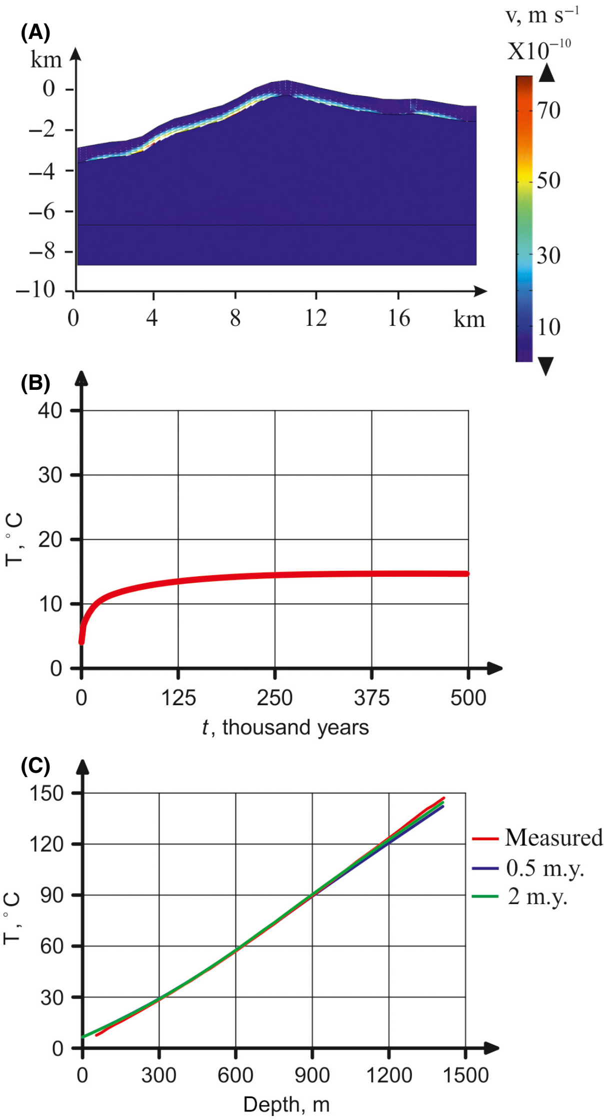

Fig. 11. (A) Darcy velocity field for Model D, showing upflow at the site of the LCHF and in a small hill to the north of the location of IODP Hole 1309D (Fig. 2), with downflow at the site of the borehole. (B) Vent temperatures for Model D. Note that the initial stage of unstable venting is not seen in this model. (C) Observed and modelled temperature profiles in IODP Hole 1309D.

on this process have not been explicitly addressed by numerical modelling.

We have modelled much shorter wavelength topography than other authors, and seafloor topography has a profound effect on circulation. Our initial condition of a constant heat flux with a conductive gradient throughout ensures that isotherms are higher beneath the Massif, and the first stable vents always form near the crest. Vents may migrate with time but are never located in the transform valley except sometimes on the edge of the model. Topography is therefore a driving force for circulation in our models with the reverse effect to subaerial systems where hydraulic head drives fluid from high to low ground. However, comparison of models B and C shows that permeability structure is more important than topography in controlling the vent location. We have not used a constant temperature lower boundary condition (as generally used in magmatic-hydrothermal modelling) in our models, but it is likely that this would decrease the topographic effect due to the higher heat flow where isotherms are compressed. This is consistent with the observation that black smoker vents often show no clear relationship to seafloor topography.

Importance of permeability structure in stabilizing long-term venting

Our modelling shows that the existence of a near-conductive thermal gradient in a borehole only 5 km north of the LCHF can only be explained by a large lateral permeability contrast between the area beneath the vent and that beneath the borehole. A steeply dipping boundary between high and low permeability attracts upwelling fluid and stabilizes vent positions by creating a lateral conductive boundary layer. In our models, the vents can be stabilized at near constant temperature similar to the LCHF for periods of over 0.5 m.y. Comparison of Figs 5 and 8 shows that the vents stabilize more quickly in model B than in model A with less oscillation of temperature. We tested two locations for the permeability change. A location corresponding to the inferred boundary between gabbro and serpentinite based on seismic tomography (Canales *et al.* 2008; Henig *et al.* 2012) stabilized the vent but somewhat to the north of the Lost City vent field, and can therefore be rejected. This location is also close to a fault proposed by Karson *et al.* (2006) which is mildly seismically active (Collins *et al.* 2012). This fault does not appear to influence circulation. A domain boundary closer to the vent site was more successful and probably reflects active faulting along the southern crest of the Massif, as suggested by Früh-Green *et al.* (2003), Kelley *et al.* (2005) and Karson *et al.* (2006), and observed by Collins *et al.* (2012). At high levels, the vent sites are likely controlled by open fractures which cannot be accurately represented in our porous flow models. At greater depths, however, fluid is likely to occur in a network of narrow fractures that can be approximated successfully by a continuum model, and we believe that the general features of the upflow zone are likely to be accurate. It is also likely that 3-D flow is important, probably to some extent confined within a predominantly E–W trending fault network. In this case, the stable location of the LCHF may be controlled either by fault intersections (Früh-Green *et al.* 2003) or perhaps by topography along the length of the fault zone. The 2-D nature of our models is clearly a limitation, but all hydrothermal systems are 3-D, and despite this, many features of 3-D models are also seen in 2-D, for example Coumou *et al.* (2006, 2009). We have run some preliminary models with a permeable fault slot in a 3-D topographic massif (Titarenko & McCaig 2014a, and in prep.). Vents tend to form in the highest topography within the slot.

Permeability values, depth of circulation and vent temperatures

Circulation at Lost City can be achieved at permeability values of 10^{-14}–10^{-15} m^2, which are modest compared to those normally used in black smoker systems (Driesner 2010). We have run models at 10^{-16} m^2 where circulation is sluggish and slow to establish itself. The threshold for circulation in our models is about 5×10^{-17} m^2. Figures 5 and 8 show that vent temperatures are lower in model B14 than in A14, and consistently lower at higher permeability (Figs 8 and 10). This reflects the greater efficiency of the system at higher permeability (higher Rayleigh number), with faster flowing fluid transporting the same amount of heat at lower temperature. Model B14 removes advective heat from a smaller proportion of the basal boundary condition than model A14. This effect is also seen when models B14 and C14 are compared (Fig. 10). Temperatures after 0.5 m.y of circulation are 5.5% higher in model C14. This model has about 6% more boundary length in contact with the conductive regime than model B14, suggesting that this is the main control. In our preliminary models involving a permeable 3-D fault slot 1 to 2 km wide (Titarenko & McCaig 2014a), vent temperatures are invariably higher than in model B at a given permeability. The fault slot gives the maximum contact area with the conductive regime. In view of these effects, it is surprising that final vent temperatures are similar in models A15 and B15, perhaps reflecting competing effects of advective domain size and flow velocity.

Depth of circulation has an important effect on vent temperature in constant heat flow models. In the thin layer model (model D), maximum vent temperatures at a permeability of 3×10^{-14} m^2 are only 14°C. Although we anticipate higher temperatures at lower permeability values, it is not possible for vent temperatures to exceed temperatures at 750 mbsf in the conductive steady state (about 75°C). Similarly, with a thickness of 4 km for the basal domain 3 in model B, giving depths of circulation beneath the LCHF of about 5 km, temperatures after 0.5 m.y. are about 12% lower than for a circulation depth of 7 km (Fig. 10). Note, however, that the assumption made by Seyfried *et al.* (2015) of circulation to depths only 750 m below the LCHF is not consistent with our modelling.

Our models place important constraints on the *in situ* permeability of gabbro exposed on the seafloor, and on fractured serpentinite. Gabbro permeability must be less than 5×10^{-17} m^2, with the exception of a shallow layer (<750 m depth, modelled in Fig. 11) that must be more permeable to explain the detailed thermal profile in the borehole (Titarenko & McCaig 2014b and in prep.). Measurements in gabbro at shallower levels in ODP Hole 735b (Becker 1991) are mainly greater than this, but there are no estimates for gabbro at depths >600 mbsf. Similar values have been estimated for diabase in the deeper parts of ODP Hole 504b (Becker *et al.* 1989). Permeability beneath the LCHF is unlikely to be greater than 10^{-14} m^2, or long-term vent temperatures would likely be too low. Of course it is likely that permeability has been transient in the system, controlled by a balance between enhancement due to fault movement and perhaps reactions, and reduction due to occlusion of porosity by mineral growth. Our models are not capable of addressing this other by arbitrary means, and we have not attempted this. In general, we can say that if the depth of circulation remains the same, enhanced permeability is likely to reduce vent temperature, while lower permeability (above the threshold for circulation) will lead to higher temperature vents. Future work may reveal temperature time-series in the deposits of Lost City, and this would be valuable.

Heat source and temperatures within the hydrothermal system

In all our models, an initial transient phase of high temperature venting removes the conductive heat stored in the Massif by our initial condition. This phase of venting is not considered significant for the LCHF. It is followed by a lengthy period of gradually declining vent temperature, which is close to observed values in models B and C. In model B, the borehole temperature first rises slightly and then falls, showing that the hydrothermal circulation initially adds heat to the conductive regime beneath the borehole, and then removes it. We consider this second phase to indicate a strong control from the steep conductive boundary layer between domains 1 and 2.

We have not included heat of serpentinization in our models, as the effects of this have been modelled previously (Lowell & Rona 2002; Emmanuel & Berkowitz 2006). As pointed out by Allen & Seyfried (2004), it is hard to constrain when and where the heat would be released, and to have a significant effect serpentinization needs to occur continuously over the lifetime of circulation, which is much shorter than the lifetime of the Massif. The maximum amount of heat that could be released by full serpentinization of domain 1, model B, is about 10^{16} J using a latent heat value of 2.5×10^5 J kg^{-1} (Fyfe & Lonsdale 1981). This is very similar to the amount of heat supplied through the basal boundary condition of domain 1 in our model over the 120 000 year estimated lifetime of the LCHF. However, Boschi *et al.* (2006) showed that talc–tremolite schists in the detachment fault zone overprint serpentine, a relationship also observed in IODP Hole 1309B (Blackman *et al.* 2011). The talc–tremolite schists must have formed when the detachment fault was well below the seafloor (McCaig *et al.* 2010), at least 0.5 m.y. ago. Hence, significant serpentinization must have occurred prior to the current Lost City phase, and it is also unlikely that serpentinization has everywhere gone to completion. The actual contribution of heat from serpentinization to the LCHF is certainly less than the estimate above, and the actual value cannot be constrained. Our models show that our basal heat flow value is sufficient to drive a long-lived hydrothermal system with the vent temperature of Lost City. Furthermore, our heatflow is a minimum for the true heatflow into the Massif, based on the average thermal gradient in the borehole. Blackman *et al.* (2014) have estimated a higher value of 0.258 W m^{-2} based on the gradient in the lower 750 m of the borehole, and due to topographic effects, the actual value is probably higher (Titarenko & McCaig 2014b and in prep.). Heat of serpentinization is not therefore necessary to drive such a system, although some contribution is probable. Similarly, there will be a small contribution from radioactive heat production in the gabbro, which we have also neglected. We have shown that adding heat in the form of additional basal heatflow increases the vent temperature, and it is likely that adding heat of serpentinization will do the same. Increasing permeability or decreasing the depth of the permeable zone will decrease vent temperatures. Our purpose is not to find a unique set of parameter values that uniquely explain LCHF vent temperatures, but to show that an appropriate permeability structure can stabilize venting in a single location with temperatures in the right range. During the phase of stable venting, upward flow is slow compared to black smoker systems and significant heat is lost conductively from the upwelling fluid. Hence, temperatures at 2–3 km depth are generally much higher than estimated vent temperatures, often in the range 200–250°C. This conforms with the predictions of Allen & Seyfried (2004), Foustoukos *et al.* (2008) and Seyfreid *et al.* (2015) based on geochemical modelling. Allen & Seyfried (2004) predicted that little or no active serpentinization is occurring along the flow path. Nevertheless, the high H_2 content of the fluid indicates serpentinization (Proskurowski *et al.* 2006, 2008). The models show that vent fluids tend to have moved along a narrow range of flow paths, which are probably fully serpentinized. In other parts of the model, slower moving fluids recirculate and never reach the vents. Active serpentinization is probably occurring in these low-flux backwaters of the system, with H_2 diffusing into the high-flux zones.

Our models can be used to predict the limits of subseafloor biosphere in the vicinity of the LCHF, based on a threshold of 120°C (Kashefi & Lovley 2003). In the conductive regime around the borehole, the limit is at about 1.2 km below seafloor, and this is a very robust value. In the venting region, it should be very shallow, due to the rapid increase in fluid temperature with depth. Beneath the transform valley or in any region of recharge, the limit of subseafloor biosphere is essentially the base of the hydrothermal system and is therefore as deep as the high permeability that allows circulation. In our models, this is quite arbitrary, but circulation to a depth of several km beneath the crest of the Massif is needed to reproduce vent temperatures over long periods of time.

CONCLUSIONS

In this paper, we have shown that it is possible to drive the Lost City hydrothermal system solely with a modest basal heat flow; additional heat sources such as serpentinization are not necessary to maintain the circulation, although they could contribute. Its location and properties can be explained by the topography, and by the specific permeability structure under the Atlantis Massif. If our assumption of approximately constant heatflow into the Massif is correct, there needs to be a deep enough permeable domain beneath the vents to allow fluid to extract heat from hotter layers. The stabilization of Lost City in the same place for long periods is assisted by a lateral conductive boundary layer into a low permeability, conductive regime. Such conditions may not occur in all similar Massifs, perhaps explaining why Lost City remains a unique system in terms of its temperature and longevity. We have also shown that the permeability of the gabbro domain sampled by IODP Hole U1309D is very low ($<5 \times 10^{-17}$ m^2 below 750 m depth), and vent fields of Lost City temperature and longevity are unlikely to be hosted in gabbro unless controlled by active faults. The intrinsic permeability of serpentinized peridotite beneath the LCHF is less certain, but the bulk permeability including faults and fractures is likely to be between 10^{-14} and 10^{-15} m^2.

Notation

$\rho_f(T)$ density of water in [kg m^{-3}].
ρ_p density of the porous material in [kg m^{-3}].
k_f thermal conductivity for water in [W $m^{-1}\cdot K$].
$k_p(T)$thermal conductivity for the porous material in [W $m^{-1}\cdot K$].
ε porosity.
$p(T)$ pressure of water in [Pa].
$\mathbf{v}$ Darcy velocity field in [m sec^{-1}].
$\mathbf{g}$ gravity vector.
$k(T)$ permeability of the material in [m^2].
$\mu(T)$ water viscosity in [Pa·sec].
$c_p(T)$ heat capacity for water in [J $kg^{-1}\cdot K$].
$c_{pp}(T)$ heat capacity for porous material in [J $kg^{-1}\cdot K$].

ACKNOWLEDGEMENTS

Greg Houseman and Joe Cann are thanked for many helpful discussions in the course of this work. Donna Blackman provided a topographic data file and gave advice on sea bottom temperatures together with Gilles Guerin. Fabrice Fontaine advised on hydrothermal modelling. Taras Gerya, Gretchen Früh-Green and an anonymous reviewer helped improve a previous version of the manuscript, together with two anonymous Geofluids reviewers. This work was supported by NERC Grant NE/I015035/1. Note that since Comsol Multiphysics is a commercial code, original data for this paper cannot be accessed. However, the models can be regenerated with a Comsol Multiphysics licence using the input parameters given in this paper.

REFERENCES

Allen DE, Seyfried WE (2004) Serpentinization and heat generation: constraints from Lost City and rainbow hydrothermal systems. *Geochimica et Cosmochimica Acta*, **68**, 1347–54.

Anderko A, Pitzer KS (1993) Equation-of-state representation of phase-equilibria and volumetric properties of the system NaCl-H_2O above 573 K. *Geochimica et Cosmochimica Acta*, **57**, 1657–80.

Anderson BW, Coogan LA, Gillis KM (2012) The role of outcrop-to-outcrop fluid flow in off-axis oceanic hydrothermal systems under abyssal sedimentation conditions. *Journal of Geophysical Research-Solid Earth*, **117**, B05103.

Becker K (1991) In-situ bulk permeability of oceanic gabbros in Hole 735B, ODP Leg 118. Proc., scientific results, ODP, Leg 118, fracture zone drilling on the Southwest Indian Ridge, 333–47.

Becker K, Sakai H, Adamson AC, Alexandrovich J, Alt JC, Anderson RN, Bideau D, Gable R, Herzig PM, Houghton S, Ishizuka H, Kawahata H, Kinoshita H, Langseth MG, Lovell MA, Malpas J, Masuda H, Merrill RB, Morin RH, Mottl MJ, Pariso JE, Pezard P, Phillips J, Sparks J, Uhlig S (1989) Drilling deep into young oceanic crust, Hole 504b, Costa Rica Rift. *Reviews of Geophysics*, **27**, 79–102.

Blackman DK, Cann JR, Janssen B, Smith DK (1998) Origin of extensional core complexes: evidence from the Mid-Atlantic Ridge at Atlantis Fracture Zone. *Journal of Geophysical Research-Solid Earth*, **103**, 21315–33.

Blackman DK, Karson JA, Kelley DS, Cann JR, Früh-Green GL, Gee JS, Hurst SD, John BE, Morgan J, Nooner SL, Ross DK, Schroeder TJ, Williams EA (2002) Geology of the Atlantis Massif (Mid-Atlantic Ridge, 30 degrees N): implications for the evolution of an ultramafic oceanic core complex. *Marine Geophysical Researches*, **23**, 443–69.

Blackman DK, Ildefonse B, John BE, Ohara Y, Miller DJ, MacLeod CJ, Scientists E (2006) Oceanic core complex formation, atlantis massif. In *Proceedings of the Integrated Ocean Drilling Program*, Volume 304/305: Integrated Ocean Drill. Program Manage. Int. Inc., College Station, TX. http://publications.iodp.org/proceedings/304_305/30405title.htm.

Blackman DK, Ildefonse B, John BE, Ohara Y, Miller DJ, Abe N, Abratis M, Andal ES, Andreani M, Awaji S, Beard JS, Brunelli D, Charney AB, Christie DM, Collins J, Delacour AG, Delius H, Drouin M, Einaudi F, Escartin J, Frost BR, Früh-Green G, Fryer PB, Gee JS, Godard M, Grimes CB, Halfpenny A, Hansen HE, Harris AC, Tamura A, Hayman NW, Hellebrand E, Hirose T, Hirth JG, Ishimaru S, Johnson KTM, Karner GD, Linek M, MacLeod CJ, Maeda J, Mason OU, McCaig AM, Michibayashi K, Morris A, Nakagawa T, Nozaka T, Rosner M, Searle RC, Suhr G, Tominaga M, von der Handt A, Yamasaki T, Zhao X (2011) Drilling constraints on lithospheric accretion and evolution at Atlantis Massif, Mid-Atlantic Ridge 30 degrees N. *Journal of Geophysical Research-Solid Earth*, **116**, B07103. doi:10.1029/2010JB007931.

Blackman DK, Slagle A, Harding A, Guerin G, McCaig AM (2013) Atlantis Massif Oceanic Core Complex: velocity, porosity, and impedance contrasts within the domal core of Atlantis Massif: faults and hydration of lithosphere during core complex evolution. *IODP Preliminary Report*, 340T.

Blackman DK, Slagle A, Guerin G, Harding A (2014) Geophysical signatures of past and present hydration within a young oceanic core complex. *Geophysical Research Letters*, **41**, 1179–86.

Boschi C, Früh-Green GL, Delacour A, Karson JA, Kelley DS (2006) Mass transfer and fluid flow during detachment faulting and development of an oceanic core complex, Atlantis Massif (MAR 30 degrees N). *Geochemistry Geophysics Geosystems*, **7**, Q01004.

Bouhifd MA, Besson P, Courtial P, Gerardin C, Navrotsky A, Richet P (2007) Thermochemistry and melting properties of basalt. *Contributions to Mineralogy and Petrology*, **153**, 689–98.

Canales JP, Tucholke BE, Xu M, Collins JA, DuBois DL (2008) Seismic evidence for large-scale compositional heterogeneity of oceanic core complexes. *Geochemistry Geophysics Geosystems*, **9**, Q08002.

Cann JR, Blackman DK, Smith DK, McAllister E, Janssen B, Mello S, Avgerinos E, Pascoe AR, Escartin J (1997) Corrugated slip surfaces formed at ridge-transform intersections on the Mid-Atlantic Ridge. *Nature*, **385**, 329–32.

Cherkaoui ASM, Wilcock WSD (1999) Characteristics of high Rayleigh number two-dimensional convection in an open-top porous layer heated from below. *Journal of Fluid Mechanics*, **394**, 241–60.

Cherkaoui ASM, Wilcock WSD (2001) Laboratory studies of high Rayleigh number circulation in an open-top Hele-Shaw cell: an analog to mid-ocean ridge hydrothermal systems. *Journal of Geophysical Research-Solid Earth*, **106**, 10983–1000.

Collins JA, Smith DK, McGuire JJ (2012) Seismicity of the Atlantis Massif detachment fault, 30 degrees N at the Mid-Atlantic Ridge. *Geochemistry Geophysics Geosystems*, **13**, Q0AG11. doi:10.1029/2012gc004210.

Coumou D, Driesner T, Geiger S, Heinrich CA, Matthai S (2006) The dynamics of mid-ocean ridge hydrothermal systems: splitting plumes and fluctuating vent temperatures. *Earth and Planetary Science Letters*, **245**, 218–31.

Coumou D, Driesner T, Geiger S, Paluszny A, Heinrich CA (2009) High-resolution three-dimensional simulations of mid-ocean ridge hydrothermal systems. *Journal of Geophysical Research-Solid Earth*, **114**, B07104. doi:10.1029/2008JB006121.

Driesner T (2010) The interplay of permeability and fluid properties as a first order control of heat transport, venting temperatures and venting salinities at mid-ocean ridge hydrothermal systems. *Geofluids*, **10**, 132–41.

Emmanuel S, Berkowitz B (2006) Suppression and stimulation of seafloor hydrothermal convection by exothermic mineral hydration. *Earth and Planetary Science Letters*, **243**, 657–68.

Fisher AT, Becker K (2000) Channelized fluid flow in oceanic crest reconciles heat-flow and permeability data. *Nature*, **403**, 71–4.

Fontaine FJ, Wilcock WSD (2007) Two-dimensional numerical models of open-top hydrothermal convection at high Rayleigh and Nusselt numbers: implications for mid-ocean ridge hydrothermal circulation. *Geochemistry Geophysics Geosystems*, **8**, Q07010.

Foustoukos DI, Savov IP, Janecky DR (2008) Chemical and isotopic constraints on water/rock interactions at the Lost City hydrothermal field, 30 degrees N Mid-Atlantic Ridge. *Geochimica et Cosmochimica Acta*, **72**, 5457–74.

Früh-Green GL, Kelley DS, Bernasconi SM, Karson JA, Ludwig KA, Butterfield DA, Boschi C, Proskurowski G (2003) 30 000 years of hydrothermal activity at the Lost City vent field. *Science*, **301**, 495–8.

Fyfe WS, Lonsdale P (1981) Ocean floor hydrothermal activity. In: *The Sea, Vol. 7, The Oceanic Lithosphere* (ed. Emiliani C), pp. 589–638. Wiley, New York.

Graham MD, Steen PH (1994) Plume formation and resonant bifurcations in porous-media convection. *Journal of Fluid Mechanics*, **272**, 67–89.

Grimes CB, John BE, Cheadle MJ, Wooden JL (2008) Protracted construction of gabbroic crust at a slow spreading ridge: constraints from Pb-206/U-238 zircon ages from Atlantis Massif and IODP Hole U1309D (30 degrees N, MAR). *Geochemistry Geophysics Geosystems*, **9**, Q08012.

Harris RN, Fisher AT, Chapman DS (2004) Fluid flow through seamounts and implications for global mass fluxes. *Geology*, **32**, 725–8.

Hayba DO, Ingebritsen SE (1997) Multiphase groundwater flow near cooling plutons. *Journal of Geophysical Research-Solid Earth*, **102**, 12235–52.

Henig AS, Blackman DK, Harding AJ, Canales JP, Kent GM (2012) Downward continued multichannel seismic refraction analysis of Atlantis Massif oceanic core complex, 30 degrees N, Mid-Atlantic Ridge. *Geochemistry Geophysics Geosystems*, **13**, Q0AG07. doi:10.1029/2012gc004059.

Ildefonse B, Blackman DK, John BE, Ohara Y, Miller DJ, MacLeod CJ, Integrated Ocean Drilling P (2007) Oceanic core complexes and crustal accretion at slow-spreading ridges. *Geology*, **35**, 623–6.

Ingebritsen SE, Hayba DO (1994) Fluid-flow and heat transport near the critical point of H_2O. *Geophysical Research Letters*, **21**, 2199–202.

Ingebritsen SE, Geiger S, Hurwitz S, Driesner T (2010) Numerical simulation of magmatic-hydrothermal systems. *Reviews of Geophysics*, **48**, RG1002. doi:10.1029/2009rg000287.

Karson JA, Früh-Green GL, Kelley DS, Williams EA, Yoerger DR, Jakuba M (2006) Detachment shear zone of the Atlantis Massif core complex, Mid-Atlantic Ridge, 30 degrees N. *Geochemistry Geophysics Geosystems*, **7**, Q06016. doi:10.1029/2005GC001109.

Kashefi K, Lovley DR (2003) Extending the Upper Temperature Limit for Life. *Science*, **301**, 934.

Kawada Y, Seama N, Urabe T (2011) The role of seamounts in the transport of heat and fluids: relations among seamount size, circulation patterns, and crustal heat flow. *Earth and Planetary Science Letters*, **306**, 55–65.

Kelley DS, Shank TM (2010) Hydrothermal systems: a decade of discovery in slow spreading environments. In: *Diversity of Hydrothermal Systems on Slow Spreading Ocean Ridges* (eds Rona PA, Devey CW, Dyment J, Murton BJ), **188**, pp. 369–407. Amer Geophysical Union, Washington.

Kelley DS, Karson JA, Blackman DK, Früh-Green GL, Butterfield DA, Lilley MD, Olson EJ, Schrenk MO, Roe KK, Lebon GT, Rivizzigno P, Party ATS (2001) An off-axis hydrothermal vent field near the Mid-Atlantic Ridge at 30 degrees N. *Nature*, **412**, 145–9.

Kelley DS, Karson JA, Früh-Green GL, Yoerger DR, Shank TM, Butterfield DA, Hayes JM, Schrenk MO, Olson EJ, Proskurowski G, Jakuba M, Bradley A, Larson B, Ludwig K, Glickson D, Buckman K, Bradley AS, Brazelton WJ, Roe K, Elend MJ, Delacour A, Bernasconi SM, Lilley MD, Baross JA, Summons RT, Sylva SP (2005) A serpentinite-hosted ecosystem: the lost city hydrothermal field. *Science*, **307**, 1428–34.

Kimura S, Schubert G, Straus JM (1986) Route to chaos in porous-medium convection. *Journal of Fluid Mechanics*, **166**, 305–24.

Lowell RP, Rona PA (2002) Seafloor hydrothermal systems driven by the serpentinization of peridotite. *Geophysical Research Letters*, **29**, 26-1–26-4. doi:10.1029/2001GL014411.

Ludwig KA, Shen CC, Kelley DS, Cheng H, Edwards RL (2011) U-Th systematics and Th-230 ages of carbonate chimneys at the Lost City Hydrothermal Field. *Geochimica Et Cosmochimica Acta*, **75**, 1869–88.

McCaig AM, Harris M (2012) Hydrothermal circulation and the dike-gabbro transition in the detachment mode of slow seafloor spreading. *Geology*, **40**, 367–70.

McCaig AM, Delacour A, Fallick AE, Castelain T, Früh-Green GL (2010) Detachment fault control on hydrothermal circulation systems: interpreting the subsurface beneath the TAG hydrothermal field using the isotopic and geological evolution of oceanic core complexes in the Atlantic. In: *Diversity of Hydrothermal Systems on Slow-Spreading Ocean Ridges* (eds Rona PA, Devey C, Dyment J, Murton B), **108**, pp. 207–40. AGU, Washington, DC.

Pitzer KS, Peiper JC, Busey RH (1984) Thermodynamic properties of aqueous sodium chloride solutions. *Journal of Physical and Chemical Reference Data*, **13**, 1–102.

Proskurowski G, Lilley MD, Kelley DS, Olson EJ (2006) Low temperature volatile production at the Lost City Hydrothermal Field, evidence from a hydrogen stable isotope geothermometer. *Chemical Geology*, **229**, 331–43.

Proskurowski G, Lilley MD, Seewald JS, Früh-Green GL, Olson EJ, Lupton JE, Sylva SP, Kelley DS (2008) Abiogenic hydrocarbon production at Lost City hydrothermal field. *Science*, **319**, 604–7.

Schardt C, Large RR (2009) New insights into the genesis of volcanic-hosted massive sulfide deposits on the seafloor from numerical modeling studies. *Ore Geology Reviews*, **35**, 333–51.

Schardt C, Large R, Yang JW (2006) Controls on heat flow, fluid migration, and massive sulfide formation of an off-axis hydrothermal system - The Lau basin perspective. *American Journal of Science*, **306**, 103–34.

Schroeder T, John BE (2004) Strain localization on an oceanic detachment fault system, Atlantis Massif, 30 degrees N, Mid-Atlantic Ridge. *Geochemistry Geophysics Geosystems*, **5**, Q11007.

Seipold U (1998) Temperature dependence of thermal transport properties of crystalline rocks - a general law. *Tectonophysics*, **291**, 161–71.

Seyfried WE Jr, Pester NJ, Tutolo BM, Ding K (2015) The Lost City hydrothermal system: constraints imposed by vent fluid chemistry and reaction path models on subseafloor heat and mass transfer processes. *Geochimica et Cosmochimica Acta*, **163**, 59–79.

Titarenko S, McCaig AM (2014a) Hydrothermal circulation in fault slots with topography. *EGU General Assembly Conference Abstracts*, **16**, 10934.

Titarenko S, McCaig AM (2014b) Constraints on the Lost City Hydrothermal System from borehole thermal data; 3-D models of heat flow and hydrothermal circulation in an oceanic core complex. *AGU Fall Meeting Abstracts*, **1**, 4729.

Wagner W, Kretzschmar H-J (2008) *International Steam Table - Properties of Water and Steam Based on the Industrial Formulation IAPWS-IF97*, 2nd edn. Springer-Verlag, Berlin.

Wilcock WSD (1998) Cellular convection models of mid-ocean ridge hydrothermal circulation and the temperatures of black smoker fluids. *Journal of Geophysical Research-Solid Earth*, **103**, 2585–96.

SUPPORTING INFORMATION

Additional Supporting Information may be found in the online version of this article:

Figure S1. Temperature gradient measured in IODP 340T (Blackman *et al.* 2013).

Figure S2. Density (blue line) and viscosity (green line) profiles of pure water at 500 bars pressure (Wagner & Kretzschmar 2008).

Figure S3. Thermal conductivity (blue line) and heat capacity (green line) for rocks used in this study. Room temperature conductivity is the average of gabbro and olivine gabbro/troctolite from Blackman *et al.* (2006). Temperature dependence from Bouhifd *et al.* (2007) and Seipold (1998).

Figure S4. Example of our temperature dependent permeability function. Permeability below 800°C is variable, depending on model and domain.

Table S1. Comparison of permeability domains and mesh size for different models. For all models the maximum element size is 198 m.

Table S2. Comparison of pure water properties along a 500 bar isobar, and at variable pressure reflecting the top and base of the permeable zone.

Movie S1. Temperature evolution in model A14, in which the permeability of domains 1 and 2 (Fig. 2) is 10^{-14} m^2, while that of domain 3 is 10^{-22} m^2.

Movie S2. Temperature evolution of model A15 in which domains 1 and 2 (Fig. 2) both have permeability 10^{-15} m^2.

Movie S3. Thermal evolution of model B14. Model B15 (not shown) displays similar flow patterns to B14, but with a slower onset of circulation and less instability at <50 k years.

Movie S4. Thermal evolution in model C14.

Appendix S1. Model development and numerical parameters.